

Modeling afterslip and aftershocks following the 1992, Landers Earthquake.

H. Perfettini

Institut de Recherche pour le Développement/Observatoire Midi-Pyrénées, Toulouse,
France.

J.-P. Avouac

Tectonics Observatory, Division of Geological and Planetary Sciences, California
Institute of Technology.

Short title: AFTERSLIP MODEL OF THE LANDERS EARTHQUAKE

Abstract. One way to probe the rheology of the lithosphere and fault zones consists in analyzing the temporal evolution of deformation following a large earthquake. In such a case, the lithosphere responds to a known stress change which can be assessed from source models constrained from seismology or geodesy. Here, we model the postseismic response of a fault zone which is assumed to obey a rate-strengthening rheology. The model predicts well the near field geodetic measurements of postseismic deformation following the $M_w = 7.3$, 1992, Landers earthquake. Based on this modeling we determine the pre-seismic velocity of the creeping patch to 7 mm/yr and estimate the rheological parameter $a\sigma = 0.6$ MPa. We show that aftershocks and afterslip follow the same temporal evolution and demonstrate that the spatial distribution of aftershocks is consistent with the idea that they are driven by reloading of the seismogenic zone by afterslip at depth.

Keywords: 1992 Landers earthquake, Afterslip, Aftershocks, Postseismic deformation, GPS

1. Introduction

Aftershocks and postseismic deformation are most common manifestations of stress relaxation following large earthquakes. Postseismic relaxation can result from ductile deformation distributed within the lower crust and upper mantle [Pollitz *et al.*, 1998; Deng *et al.*, 1998], pore fluids redistribution [Peltzer *et al.*, 1998; Bosl and Nur, 2002], and localized shear due to ductile fault zone deformation or frictional sliding, here refer to as afterslip. Afterslip can occur either up-dip or down-dip of the ruptured zone [Smith and Wyss, 1968; Marone *et al.*, 1991; Zweck *et al.*, 2002]. Identifying the respective contribution of these various mechanisms is generally a challenge. In some cases, aftershocks and geodetic deformation follow the same temporal evolution [Perfettini and Avouac, 2004; Perfettini *et al.*, 2005], an observation which seems to hold for the $M_w = 7.3$, 1992 Landers earthquake. Indeed, we observe that the cumulated number of aftershocks with $M_w > 2$ [Hauksson *et al.*, 2003] within about 15 km from the ruptured faults follow the same time evolution than geodetic strain as documented from near field measurements (Figure 1) [Savage and Svarc, 1997]. The close agreement between those two curves is unexpected if the aftershocks were the delayed response to the co-seismic step increase of stress as commonly admitted [Dieterich, 1994; Stein, 1999]. This mechanism has been shown to provide a reasonable explanation of the temporal evolution and spatial distribution of distant aftershocks, located more than 5 km away from the main ruptured fault [Gross and Kisslinger, 1997], but it should be noticed that the correlation in Figure 2 heavily depends on the near faults seismicity, less than

5 km from the ruptured faults, which represent about 95 % of the aftershocks [*Liu et al.*, 2003]. The correlation in Figure 2 suggests that the time evolution of near-fault aftershocks and of postseismic deformation are linked.

We start by reviewing evidences for deep afterslip following the Landers earthquake (section 2) and next present our modeling approach (section 3). We then compare the predictions of the model with postseismic deformation (section 4) and with the spatial and temporal evolution of aftershocks (section 5).

Figure 1.

Figure 2.

2. Evidence for deep afterslip following the Landers earthquake.

Postseismic deformation following the $M_w = 7.3$, 1992 Landers earthquake was particularly well documented from geodetic measurements, including campaign GPS measurements by USGS and continuous GPS measurements by the SCIGN network (Figure 1) [*Shen et al.*, 1994; *Bock et al.*, 1997; *Savage and Svarc*, 1997; *Savage et al.*, 2003], and from SAR interferometry [*Peltzer et al.*, 1996, 1998; *Massonnet et al.*, 1996; *Fialko*, 2004a]. To the first order GPS deformation follows approximately the same time evolution as the aftershocks (Figure 2). It has been found that the near field GPS measurements require some component of postseismic strain localized below the ruptured fault segments [*Savage et al.*, 2003; *Fialko*, 2004a]. InSAR measurements covering the period between the 1992 Landers earthquakes and the 1999 Hector Mine earthquakes show that the dominant signal is due to poro-elastic effects but also near fault displacement gradients suggesting a relatively localized zone of post-seismic deformation [*Peltzer et al.*, 1996, 1998]. Those InSAR measurements show in fact a

very limited effect of viscous relaxation over that time period [*Fialko, 2004a*]. The most plausible model satisfying all data involves a combination of afterslip at depths deeper than about 10-15 km, mostly below the ruptured fault zone determined from the inversion of the near field GPS data, and poroelastic deformation of the elasto-brittle crust [*Savage and Swarc, 1997; Fialko, 2004a*]. No evidence for shallow afterslip was found in that particular case.

In theory, postseismic deformation at mid-crustal to lower crustal depths could reflect either a ductile behavior or brittle creep, a deformation process equivalent to rate-strengthening friction [*Hearn et al., 2002; Montési, 2004; Savage et al., 2005*]. Detailed analysis of some case studies including the 1999 Izmit earthquake [*Hearn et al., 2002; Savage et al., 2005*], the 1999 Chi-Chi earthquake [*Perfettini and Avouac, 2004; Hsu et al., 2002; Savage et al., 2005*] or the 2003 Tokachi-oki earthquake [*Miyazaki et al., 2004*] have advocated for afterslip governed by brittle creep, or equivalently frictional rate-strengthening friction. This mechanism, in which the shear stress on the creeping fault, or equivalently within the deforming gouge, depends on the logarithm of the sliding velocity (or strain rate), leads approximately to a 1/time decay of postseismic velocity [*Marone et al., 1991; Perfettini and Avouac, 2004*]. These observations are consistent with the view that, due to the increasing temperature with depth, fault friction would change from rate-weakening in the Seismogenic Fault Zone (SFZ) to rate strengthening at greater depth [*Rice and Gu, 1983; Scholz, 2002; Marone, 1998; Blanpied et al., 1995*]. The transition depth roughly corresponds to the isotherm 250 °C [*Blanpied et al., 1995*], a temperature reached at a depth of 15 km in the San Andreas fault

system [*Lachenbruch and Sass, 1973*]. The area below the SFZ will be called the Brittle Creep Fault Zone (BCFZ).

3. Modeling afterslip

3.1. Principles

We assume here that afterslip following the Landers earthquake resulted from brittle creep in the BCFZ and estimate the rheological parameters required to fit the geodetic observations. For simplicity we will assume that brittle creep is localized on a fault obeying a rate-strengthening friction law:

$$\tau = \sigma[\mu_* + a \log(\frac{V}{V_*})], a > 0 \quad (1)$$

where τ and σ are respectively the shear stress and effective normal stress acting on the BCFZ and V_* is a reference slip rate. The frictional parameters are the friction at the reference velocity, $\sigma\mu_*$, and $A \equiv a\sigma$ which characterizes the dependency of friction on the slip rate and is the only parameter determining the dynamic of the BCFZ.

According to (1) the friction coefficient τ/σ is a linear function of $\log(\frac{V}{V_*})$ with slope $A = a\sigma$. In previous investigations of fault zone rheology, one approach has been to invert the geodetic data for the slip history on the fault and compute the varying shear and normal stresses during postseismic relaxation [*Miyazaki et al., 2004*]. This approach does not take advantage of the fact that the co-seismic stress change can be assessed. Also, the time evolution of slip is highly dependent on the parameters of the inversion. Here, we use a different approach by predicting the time evolution of

afterslip from a forward dynamical model. A similar approach has been adopted to model postseismic deformation following the 1999 Izmit earthquake, based on a Finite Element Model [Hearn *et al.*, 2002]. Here we rather use an analytical formulation using the theory of dislocations embedded in an elastic half space [Okada, 1992]. The model is simple enough that it can be inverted for the frictional parameters. Given that the signature of afterslip is mainly seen in the near field GPS measurements from USGS [Savage and Svarc, 1997; Fialko, 2004a] we will only use these data in our inversion. We thus neglect possible trade-offs with other relaxation mechanisms.

Figure 3.

3.2. Numerical implementation

In practice, we have used the fault geometry (Figure 1) and co-seismic slip distribution (Figure 3) obtained by Fialko [2004b]. This fault model consist of 357 rectangular fault segments extending vertically from the surface to a depth of 15 km. We assume that afterslip occurred in the BCFZ, i.e., along the down-dip continuation of the ruptured fault, say at a depth of $z_0 = 15.5$ km in order to avoid stress singularities at the bottom of the SFZ ($z = 15$ km). Afterslip results from the frictional response of the BCFZ to the co-seismic stress change induced by slip of the SFZ. The BCFZ extends from z_0 to $z_0 + W_{bcfz}$, where W_{bcfz} is the down-dip extent of the BCFZ and is discretized into $n_d = W_{bcfz}/dw$ cells along depth and $n_s = n/n_d$ cells along strike with $dl = 3$ km and $dw = 2.5$.

In reality it is probable that postseismic creep occurred at shallower depths than z_0 and eventually the creeping zone could overlap with the seismically ruptures zone

because of the possible propagation of the seismic rupture into the BCFZ [Rice, 1993]. The geodetic data do not provide much constraint on that issue. Also at depth deeper than z_0 it may be assumed that the fault zone was presumably slipping aseismically at a relatively constant rate, V_0 , prior to the Landers earthquake.

The balance of stresses computed in the center of cell i among $n = n_s \cdot n_d$ is

$$\tau(i, t) = \tau_0(i) + \Delta\tau_{el}(i, t) - \frac{G}{2\beta}V(i, t), \quad i = 1, n, \quad (2)$$

where $\Delta\tau_{el}(i, t)$ are the shear stress changes induced by the evolution of slip on the BCFZ, assuming that the frictional resistance $\tau(i, t)$ of each cell i obeys the brittle creep rheology (Eq. 1)

$$\tau(i, t) = \sigma(i, t)[\mu_*(i) + a(i) \log(\frac{V(i, t)}{V_*(i)})], \quad i = 1, n, \quad (3)$$

where $\sigma(i)$ represents the effective normal stress on cell i . The distributions $\mu_*(i)$ and $V_*(i)$ are set homogeneous spatially, i.e., $\mu_*(i) = \mu_*$ and $V_*(i) = V_*$ with the particular choice $\mu_* = 0.6$ and $V_* = 10^{-6}$ m/s, a choice which has no effect on the dynamics of the system. The adimensional parameter $a(i) > 0$ relates changes of the creeping rate and of the applied stresses. $\mu_*(i)$ is the friction coefficient for steady state sliding at velocity $V_*(i)$ and $\tau_0(i)$ is the initial (or pre) shear stress. The term $\frac{G}{2\beta}V(i, t)$ is the radiation damping term, where G is the shear modulus set to $G = 30$ GPa, and β the shear wave velocity set to $\beta = 3$ km/s. Models considering this term are said to be quasi-dynamic [Rice, 1993] because they incorporate the elastodynamic limit result for instantaneous changes of $V(i, t)$. Using this term, infinite velocities can not be reached during the calculation.

The elastic shear stress changes induced by the evolution of slip on the BCFZ on cell i may be written

$$\Delta\tau_{el}(i, t) = \sum_{j=1}^n K(i, j)[\delta(j, t) - V_0 t], \quad i = 1, n, \quad (4)$$

where $\delta(j, t)$ is the displacement of cell j , and V_0 the loading velocity. This equation is generalized to account for normal stress changes by substituting $\Delta\tau_{el}$ by the Coulomb stress change ΔCFF [Perfettini *et al.*, 2003]. The component $K(i, j)$ of the elastic kernel represents the shear stress change induced by a unit slip on cell j in the rake direction of this cell computed in the direction of the rake of cell i , assuming a Poisson coefficient of $\nu = 0.25$ and a shear modulus of $G = 30$ GPa. The elastic kernels are computed using analytical solutions for stress and strain induced by a dislocation in an elastic half-space [Okada, 1992]. We neglect the possible temporal variations of the rake, as well as of the constitutive parameters ($\frac{da(i)}{dt} = \frac{d\mu_*(i)}{dt} = 0$) and effective normal stress ($\frac{d\sigma(i)}{dt} = 0$).

Combining Eq. (2), (3) with (4) yields after a derivation with respect to time

$$\frac{dV(i, t)}{dt} = \frac{\sum_{j=1}^n K(i, j)[V(j, t) - V_0]}{\frac{\sigma(i)a(i)}{V(i, t)} + \frac{G}{2\beta}}, \quad i = 1, n. \quad (5)$$

By combining Eq. (3) and (4), neglecting the radiation damping term and replacing the shear stress change $\Delta\tau_{el}(i, t)$ by the Coulomb stress change $\Delta CFF_{stat}(i)H(t)$, where $H(t)$ is the Heaviside function, we obtain that the initial velocity distribution is

$$V(i)^+ = V(i)^- \exp\left[\frac{\Delta CFF_{stat}(i)}{a(i)\sigma(i)}\right], \quad i = 1, n, \quad (6)$$

where $\Delta CFF_{stat}(i)$ is the coseismic static Coulomb stress change computed using a

co-seismic slip model.

To reduce the number of parameters of the model, we assume that the V^- distribution is homogeneous spatially so that $V(i)^- = V^-$ everywhere on the BCFZ. A first guess would be to assume that $V^- = V_0$, an assumption that would be true if the static stress field was suddenly applied on a BCFZ sliding in steady state. In reality, the static stress field is not applied instantaneously and is preceded by a dynamic stress field [Bouchon *et al.*, 1998] that is not considered in our modeling of the co-seismic phase. The other parameters of the model controlling the dynamics of the BCFZ are $a(i)\sigma(i)$ and the loading velocity V_0 . For the sake of simplicity, we assume homogeneous properties, i.e., a constant value $a(i)\sigma(i) = a\sigma$. With those assumptions, the model only depends on four parameters: The initial velocity V^- , the rheological parameter $a\sigma$, the loading velocity V_0 and the down-dip extent W_{bcfz} of the BCFZ.

For any point $\mathbf{r} = (x, y, z)$ of the elastic medium, the displacement $U_i(\mathbf{r}, t)$ along the i axis is given by

$$U_i(\mathbf{r}, t) = \sum_{j=1}^n M_{i,j}(\mathbf{r}, t) \delta_j(t), \quad (7)$$

where $M_{i,j}(\mathbf{r}, t)$ represents the displacement at \mathbf{r} in the i direction induced by a slip unit on cell j in the direction of the rake of cell j . As for the matrix $K(i, j)$, $M_{i,j}$ is computed using elastic dislocations [Okada, 1992] with a Poisson coefficient of $\nu = 0.25$ and a shear modulus of $G = 30$ GPa. This equation states that in linear elasticity, the displacement $U_i(\mathbf{r}, t)$ of point \mathbf{r} at any time t after the mainshock results from the summation of the contributions of each individual slip $\delta_j(t)$ of each cell j to the stresses applied to cell i .

4. Results of the modeling of postseismic deformation

4.1. Determination of the best fitting model

A linear array of ten GPS monuments: Oldw, Oldd, Lae4, Lae3, Lae2, Lae1, Law1, Law2, Law3 and Law4 (Figure 1) was established by the U.S.G.S across the Emerson fault segment 12 days (0.034 yr) after the Landers mainshock providing an exceptional record of postseismic deformation in the near-field [*Savage and Svarc, 1997; Savage et al., 2003*]. As in a previous work [*Savage and Svarc, 1997*], we consider the relative displacement of these ten stations relative to GPS station Sanh (Figure 1). We verify a posteriori that the model predicts a reasonable fit to the displacement of Sanh relative to stable North America.

We seek for the set of parameters ($a\sigma$, V_0 , V^- , W_{bcfz}) that minimizes the root mean square (RMS) between the modelled and observed postseismic displacements using simulated annealing combined with the downhill simplex method of Nelder and Mead [*Press et al., 1992*]. The best fitting parameters are $A = a\sigma = 6$ bar (Figure 4), $V_0 = 7$ mm/yr (Figure 5), $V^-/V_0 = 40$ (Figure 6) and W_{bcfz} is constrained to be larger than 20 km (Figure 7). We only determine a lower bound on W_{bcfz} because the model is only affected by this parameter if edge effects happen as the zone with large afterslip spreads laterally. Confidence intervals, at the 68 % confidence level, on the model parameters are determined by selecting the models yielding a RMS lower than 18 mm/yr, leading to $A = 0.6 +0.15/-0.1$ MPa, $V_0 = 7 +5/-2$ mm/yr and $V^-/V_0 = 40 +10/-10$. The best fitting model predicts reasonably well the displacements of Sanh

relative to North America (Figure 8), and the displacements measured at distant GPS stations of the SCEC network (Figure 9). A linear contribution that stands within the range of the Very Long Baseline Interferometry estimates (-5,-8, -11 mm/yr for east component and 0, 4, 8 mm/yr for the north component) has been added [*Gordon et al.*, 1993]. This is done to account for the influence of the San Andreas fault system which seems to control the pre-seismic motion of GPS stations in the Landers area [*Feigl and al.*, 1993; *Savage and Svarc*, 1997].

4.2. Interpreting the results

If the stress change was a simple step function, $V^-(i)$ should be equal to the pre-seismic slip rate, V_0 , assuming steady-state sliding at velocity V_0 prior to the mainshock. In fact, we found that the fit to the geodetic data was significantly improved if the V^- distribution is taken constant but 40 times larger than V_0 . After the co-seismic rupture, the slip rate on the BCFZ decreases as the elastic stresses in the medium are being relaxed. In the case of a single-degree of freedom system the slip rate decays approximately as $1/\text{time}$ [*Marone et al.*, 1991; *Perfettini and Avouac*, 2004]. Here, the evolution is slightly different, with a less rapid decay rate over the first few weeks, because the creeping zone spreads out with time (Figure 3). The width of the BCFZ needs to be larger than 20 km to avoid that the creeping zone reaches the down-dip limit of the modeled BCFZ over the 6 years modeled here. In reality, there must be transition at depth from a dominantly brittle creep rheology to a ductile rheology. We assume that, given the 6 year time period considered here, the effect of the ductile

Figure 4.

Figure 5.

Figure 6.

Figure 7.

Figure 8.

Figure 9.

rheology can be neglected. The best fit parameters are $A = 0.6 +0.15/-0.1$ MPa, $V^-/V_0 = 40 +10/-10$, and $V_0 = 7 +5/-2$ mm/yr (uncertainties correspond to 68 % confidence level, see section 4.1). This set of model parameters provides a relatively good fit to all the data (Figure 10) with a RMS of the order of 17 mm, somewhat larger than the estimated $1 - \sigma$ uncertainty on the geodetic measurements (estimated to $4 - 7$ mm/yr [*Savage et al.*, 2003]). Given the simplicity of the model, this adjustment is quite satisfying. Most of the misfits comes from stations to the northeast of the ruptures that may have been affected by aseismic slip triggered by the Landers mainshock or by coseismic slip of nearby aftershocks. We did not include this complexity in the model. The slip rate is a rapidly decaying function of time. Its peak value, reached at the end of coseismic rupture, is close to 0.9 km/s, a value comparable while smaller than typical seismic rupture velocities ($\simeq 1-5$ km/s). For the best fitting model parameters, it takes more than 100 yr for the mean velocity of the BCFZ to decay to V_0 .

The pre-seismic velocity is relatively well constrained to $V_0 = 7$ mm/yr (Figure 5), and is consistent with geodetic measurement ($7 - 12$ mm/yr) of interseismic strain rates across the East California Shear Zone [*Sauber et al.*, 1986; *Savage et al.*, 1990; *Sauber et al.*, 1994]. The value of $A = a\sigma$ is estimated to 0.6 MPa and is comparable to values estimated from deep afterslip following the Chi-Chi earthquake [*Perfettini and Avouac*, 2004], the Izmit earthquake [*Hearn et al.*, 2002], or some subduction events [*Miyazaki et al.*, 2004; *Perfettini et al.*, 2005] which all fall in the range 0.1-1 MPa. This value is at least one order of magnitude smaller than estimates obtained considering that σ is lithostatic and that the a parameter falls in laboratory measurements on

quartzo-feldspathic rocks ($a \simeq 10^{-2}$) [Marone, 1998]. A reasonable explanation is that over-pressured fluids may reduce the effective normal stress σ way below its lithostatic value.

If we assume $V^-/V_0 = 1$ the best RMS is only about 35 mm/yr (Figure 6) because the distribution of creeping velocity $V^+(i)$ right after the earthquake is too low. We see two possible explanations. One is that coseismic stress increase are underestimated in our model, one reason being that afterslip is assumed to occur too far from the coseismic slip (because of the arbitrariness of the choice of z_0). This feature is discussed at the end of section 5.2. Another possibility is that creep rate increases due to the effect of dynamic stress changes. This mechanism is probably a viable explanation as demonstrated from the observation that shallow surface creep can be accelerated by distant seismic events [Hudnut and Clark, 1989; Bodin et al., 1994].

Figure 10.

5. Relationship between postseismic deformation and aftershocks

5.1. Principle of the analysis

There are many observations that tend to suggest that afterslip and aftershocks are related quantities, Figure 2 being one of them. It is well known that the decay rate of afterslip scales as 1/time [Cohen, 1998; Miyazaki et al., 2004; Perfettini and Avouac, 2004]. This is to be linked to the 1/time decay of seismicity rate, known as the Omori Law. Finally, Dieterich's model of aftershocks [Dieterich, 1994] has been shown

to be mathematically identical to an aftershock model based on afterslip [*Perfettini and Avouac, 2004*], although some of the parameters of both models have different physical meaning. To compare seismicity rate to deformation rate, we will assume that both quantities have the same temporal evolution, imposed by the relaxation of the BCFZ. The proxy we will use for deformation rate at a given site \mathbf{r} of the medium is the rate of Coulomb stress change $\frac{d\Delta CFF(\mathbf{r};t)}{dt}$ induced by afterslip at this very point. This assumption comes from the observation that aftershocks rather occur in areas of increased coseismic Coulomb stress [*Stein, 1999*]. The rate of Coulomb stress change is defined as $\frac{d\Delta CFF(\mathbf{r};t)}{dt} = \frac{d[\Delta\tau(\mathbf{r};t) + \mu_0\Delta\sigma(\mathbf{r};t)]}{dt}$, where μ_0 is the coefficient of friction of the receiver fault locate in \mathbf{r} , $\Delta\tau(\mathbf{r};t)$ and $\Delta\sigma(\mathbf{r};t)$ being respectively the changes in shear and effective normal stresses (defined negative in compression) induced at point \mathbf{r} by afterslip. A default value of $\mu_0 = 0.6$ is chosen for receiver faults. To compute the changes $\Delta\tau(\mathbf{r};t)$ and $\Delta\sigma(\mathbf{r};t)$ in shear and effective normal tractions induced by the relaxation of the BCFZ requires the knowledge of the geometry and rake of the plane onto which the stress change are estimated. We resolve Coulomb stress changes on faults that reflect the tectonic setting of the Landers area (Figure 1), i.e., right-lateral vertical faults striking N340°E.

5.2. Spatial correlation

Figure 11 shows the coseismic Coulomb stress changes computed at a depth of 10 km onto right-lateral faults striking N340°E. Close to the main ruptured fault, the Coulomb stress pattern is complex. Figure 12 represents the Coulomb stress changes

induced by 0.06 yr (left) and 6 yr (right) of afterslip computed onto right-lateral faults striking N340°E at depths $z = 15$ km. Figure 13 represents the Coulomb stress changes induced by 6 yr of afterslip computed onto right-lateral faults striking N340°E at depths $z = 5, 10,$ and 15 km. At all depths, most aftershocks are located in areas of Coulomb stress increase. The lobes of increased Coulomb stress are getting larger as one approaches the surface. This feature is obvious on Figure 15 which shows Coulomb stress cross sections along profiles AA', BB', CC', and DD' of Figure 14, after 0.06 yr (left panel) and 6 yr (right panel) of afterslip, where the plotted seismicity concerns aftershocks located within 10 km of the cross section considered. Again, most of the aftershocks are located in areas of Coulomb stress increase.

The Coulomb stress change ΔCFF induced by afterslip (Figure 12) mimics the co-seismic Coulomb stress changes (Figure 11) except in the near fault zone where ΔCFF induced by the slip of the BCFZ is maximum and systematically positive while co-seismic deformation shows a complex pattern with spots of decreased Coulomb stress (Figure 11). In studies of the relationship between aftershocks and static coseismic Coulomb stress change, the near-fault domain is generally not considered, although it accounts for most of aftershocks [Liu *et al.*, 2003], because static coseismic Coulomb stress changes cannot be reliably estimated due to model uncertainties on the details of the assumed fault pattern and slip distribution [King *et al.*, 1994], but also the singularities of Okada's equations near the slipping fault plane [Okada, 1992]. So afterslip tends to increase further the Coulomb stress changes in areas already brought closer to rupture during the main shock both in the immediate vicinity of the faults

ruptures during the earthquake or farther away. For example, at the location of the hypocenter of the 1999 Hector Mine earthquake ($z \approx 5$ km), our model predicts that the Coulomb stress increased by about 0.4 bars over the 7 years following the Landers earthquake while coseismic Coulomb stress changes have been shown to be negligible [Pollitz and Sacks, 2002].

It is interesting to estimate the degree of agreement with the spatial distribution of aftershocks for both the coseismic and postseismic pattern. To do so we consider the pattern of Figures 11 and 13 (center panel), both computed at a depth of 10 km, and estimate for each cell i of size $dx.dy$ with $dx = dy = 1$ km the cumulated number $N_{cum}(i)$ of aftershocks in this cell. All the aftershocks with $M_L > 2$ occurring during a 6 year period are considered. If our computation predicts an increase in Coulomb stress in cell i , the cumulated number of aftershocks is plotted. If the predicted Coulomb stress is negative, then $-N_{cum}(i)$ is plotted. In other words, the function we are using is $sign(\Delta CFF(i)).N_{cum}(i)$ (the $sign$ function is defined such that $sign(u) = +1$ if $u > 0$ and -1 if $u < 0$). The interest of such visualization is that it gives information on the spatial agreement (or disagreement) between model predictions and data but also on the intensity of this agreement (or disagreement). Figures 17 and 16 show the result for the coseismic and postseismic pattern of Figure 11 and 12. Both the post- and co-seismic models agrees equally well with far field aftershocks but the Coseismic Coulomb stress pattern disagrees with the aftershocks distribution close to the Landers rupture. Table 1 show the percentage of events consistent with the pattern of co- and post-seismic deformation at various depths ($z = 5, 10$ and 15 km). At least 90 % of

aftershocks are located in areas of increased postseismic Coulomb stress why at most 60 % of them are located in areas of increased coseismic Coulomb stress, the discrepancy between the two models coming essentially from aftershocks near the ruptured fault. A way to increase the correlation in the coseismic case is to consider optimally oriented planes [King *et al.*, 1994]. But note that this could be equally done in the post-seismic case and that in any case, the correlation between the location of aftershocks and the pattern of Coulomb stress change induced by afterslip will still be higher than in the coseismic case.

Table 1.

To conclude this section, it is important to note that a better agreement between the model and the spatial distribution of aftershocks in the cross sections of Coulomb stress change (Figure 15) could be obtained setting the upper limit of the BCFZ to $z_0 = 12$ km rather than 15 km. Since the coseismic model we are using is defined down to 15 km, we decided for consistency not to overlap the SFZ and BCFZ even though the model can handle it. In nature, such an overlap is expected as confirmed by observations (e.g., [Hsu *et al.*, 2002]) and numerical modeling [Rice, 1993; Lapusta and Rice, 2003].

Figure 11.

Figure 12.

Figure 13.

Figure 14.

Figure 15.

Figure 16.

Figure 17.

5.3. Temporal correlation

If we assume that the seismicity rate $R(\mathbf{r}, t)$ at a given time t and at a given point \mathbf{r} of the medium is proportional to the Coulomb stress rate $\frac{d\Delta CFF(\mathbf{r}; t)}{dt}$ at this given point, we obtain

$$R(\mathbf{r}, t) = \alpha(\mathbf{r}) \frac{d\Delta CFF(\mathbf{r}; t)}{dt}, \quad (8)$$

where we have implicitly assumed that the constant of proportionality α is not time dependent. The parameter α characterizes the potential of the volume surrounding \mathbf{r} in producing seismicity in response to a Coulomb stress change. It is expected to depend on the density of active faults, the rheological and mechanical properties of the medium, and many other factors that are difficult to quantify. To obtain the cumulated number of earthquakes $N(\mathbf{r}, t)$, we integrate Eq. (8) with respect to time

$$N(\mathbf{r}, t) = N(0) + \alpha(\mathbf{r})[\Delta CFF(\mathbf{r}; t) - \Delta CFF(\mathbf{r}; 0)], \quad (9)$$

where $N(0)$ is the cumulated number of earthquakes at time $t = 0$, and $\Delta CFF(\mathbf{r}; 0) = 0$ since, immediately after the mainshock, the BCFZ has not yet started to load the surrounding medium. Let t_{max} be the total duration over which we consider the evolution of aftershocks. We use the round value $t_{max} = 6$ years in order to exclude in the statistics possible aftershocks of the 1999 Hector Mine earthquake. Introducing the normalized cumulated number of earthquakes

$$\overline{N}(\mathbf{r}, t) = \frac{N(\mathbf{r}, t) - N(0)}{N(\mathbf{r}, t_{max}) - N(0)}, \quad (10)$$

and the normalized Coulomb stress change

$$\overline{\Delta CFF}(\mathbf{r}; t) = \frac{\Delta CFF(\mathbf{r}; t)}{\Delta CFF(\mathbf{r}; t_{max})}. \quad (11)$$

leads to

$$\overline{N}(\mathbf{r}, t) = \overline{\Delta CFF}(\mathbf{r}; t), \quad (12)$$

after use of Eq. (9). With this simple normalization, model predictions are directly comparable to aftershocks data. Note that this normalization imposes an additional

constraint in the sense that all curves start and end at the same point.

Figure 18 shows the temporal evolution of the normalized cumulated number of aftershocks whose epicenters are located within the boxes of Figure 14. Normalized coulomb stress change are also shown and are computed at $z = 15$ km at the center of the same boxes. The correlation between those two curves is strong in box 2 where most of the afterslip occurred in our model. In box 1 the correlation is weaker but still acceptable. In box 3, the agreement between the model and the data is poor. This is not surprising since in our model, no creep occurs below box 3. In reality, such creep is expected since there are a priori no reason for the BCFZ below box 3 for not being accelerated by the occurrence of the mainshock. Having no data to constrain this issue, we have not incorporated in the model a creeping segment below box 3. Note that doing so makes the agreement between the model and the data much better.

The observation that seismicity rate follows about the same temporal evolution as afterslip (Figure 2) and that the moment of the aftershocks can only account for a very small fraction of the deformation (the cumulative scalar moment of all the aftershocks of Figure 1, excluding the $M_w = 6.5$ Big Bear event, represents only about 3 % of the moment needed to explain postseismic deformation) suggests that afterslip has governed the time evolution of aftershocks.

Figure 18.

6. Conclusion

In conclusion, postseismic deformation following the 1992 Landers Earthquake has resulted mainly from frictional afterslip (Figures 2, 9, and 10), probably at depth below

the seismogenic zone due to the transition with increasing depth from rate-weakening to rate-strengthening friction. Afterslip by reloading significantly the SFZ, provides a viable mechanism to explain both the location (Figures 12, 13, and 15) and time evolution of aftershocks (Figure 18), in particular in the immediate vicinity of the ruptured fault zone where 95 % of the aftershocks occurred.

Acknowledgments. We are very grateful to J.C. Savage and Y. Fialko for providing us some of the materials used in this study. Discussion with S. Mazzotti has helped to improve the paper. Some of the figures of this paper have been made using the Generic Mapping Tools (GMT)[*Wessel and Smith, 1998*].

References

- Blanpied, M. L., D. A. Lockner, and J. D. Byerlee, Frictional slip of granite at hydrothermal conditions, *J. Geophys. Res.*, *100*, 13,045–13,064, 1995.
- Bock, Y., et al., Southern California permanent GPS geodetic array: Continuous measurements of regional crustal deformation between the 1992 Landers and 1994 Northridge earthquakes., *J. Geophys. Res.*, *102*, 18,013–18,033, 1997.
- Bodin, P., R. Bilham, J. Behr, J. Gomberg, and K. Hudnut, Slip triggered on Southern California faults by the 1992 Joshua Tree, Landers, and Big Bear earthquakes., *Bull. Seismol. Soc. Am.*, *84*, 806–816, 1994.
- Bosl, W., and A. Nur, Aftershocks and pore fluid diffusion following the 1992 Landers earthquake, *J. Geophys. Res.*, *107*, doi:10.1029/2001JB000155, 2002.
- Bouchon, M., M. Campillo, and F. Cotton, Stress field associated with the rupture of the 1992 Landers, California, earthquake and its implications concerning the fault strength at the onset of the earthquake, *J. Geophys. Res.*, *103*, 21,091–21,097, 1998.
- Cohen, S., On the rapid postseismic uplift along Turnagain Arm, Alaska following the 1964 Prince William Sound earthquake, *Geophys. Res. Lett.*, *25*, 1213–1215, 1998.
- Deng, J., M. Gurnis, M. Kanamori, and E. Hauksson, Viscoelastic flow in the lower crust after the 1992 Landers, California earthquake, *Science*, *282*, 1689–1692, 1998.
- Dieterich, J. H., A constitutive law for rate of earthquake production and its application to earthquake clustering, *J. Geophys. Res.*, *99*, 2601–2618, 1994.
- Feigl, K., and al., Space geodetic measurements of crustal deformation in central and southern California, 1984-1992, *J. Geophys. Res.*, *98*, 21,677–21,712, 1993.

- Fialko, Y., Evidence of fluid-filled upper crust from observations of postseismic deformation due to the 1992 M_w 7.3 Landers earthquake, *J. Geophys. Res.*, *109*, doi:10.1029/2004JB002985, 2004a.
- Fialko, Y., Probing the mechanical properties of seismically active crust with space geodesy: Study of the coseismic deformation due to the 1992 M_w 7.3 (southern California) earthquake, *J. Geophys. Res.*, *109*, doi:10.1029/2003JB002756, 2004b.
- Gordon, D., C. Ma, and J. Ryan, Results from the CDP Mobile VLBI Program in the western United states, in *Contribution of Space Geodesy to Geodynamics: Crustal Dynamics, Geodyn. Ser.*, edited by D. Smith, and D. Turcotte, vol. 23, pp. 131–138. AGU, Washington D.C., 1993.
- Gross, S., and C. Kisslinger, Estimating tectonic stress rate and state with Landers aftershocks, *J. Geophys. Res.*, *102*, 7603–7612, 1997.
- Hauksson, E., W.-C. Chi, P. Shearer, and A. Michael, Comprehensive waveform cross-correlation of southern California seismograms: Part 1. Refined hypocenters obtained using the double-difference method and tectonic implications (abstract), Fall. Ann. Meeting, American Geophys. Un., Dec. 8-12, San Francisco CA, 2003.
- Hearn, E., R. Burgmann, and R. Reilinger, Dynamics of Izmit earthquake postseismic deformation and loading of the Duzce earthquake hypocenter, *Bull. Seismol. Soc. Am.*, *92*, 172–193, 2002.
- Hsu, Y.-J., N. Bechor, P. Segall, S.-B. Yu, L.-C. Kuo, and K.-F. Ma, Rapid afterslip following the 1999 Chi-Chi, Taiwan earthquake, *Geophys. Res. Lett.*, *29*, doi:10.1029/2002GL014967, 2002.

- Hudnut, K., and M. Clark, New slip along parts of the 1968 Coyote Creek fault rupture, California., *Bull. Seismol. Soc. Am.*, *79*, 451–465, 1989.
- King, G. C. P., R. S. Stein, and J. Lin, Static stress changes and the triggering of earthquakes, *Bull. Seismol. Soc. Am.*, *84*, 935–953, 1994.
- Lachenbruch, A. H., and J. H. Sass, Thermo-mechanical aspects of the San Andreas, in *Proceedings, Conference on the tectonic problems of the San Andreas fault system*, vol. 13, pp. 192–205. R. L. Kovach and A. Nur, Editors, Stanford Univ. Publ. Sci., 1973.
- Lapusta, N., and J. R. Rice, Nucleation and early seismic propagation of small and large events in a crustal earthquake model, *J. Geophys. Res.*, *108*, doi:10.1029/2001JB000793, 2003.
- Liu, J., K. Sieh, and E. Hauksson, A structural Interpretation of the Aftershock “Cloud” of the 1992 M_w 7.3 Landers earthquake, *Bull. Seismol. Soc. Am.*, *93*, 1333–1344, 2003.
- Marone, C., Laboratory-derived friction laws and their application to seismic faulting, *Annu. Rev. Earth Planet. Sci.*, *26*, 643–696, 1998.
- Marone, C. J., C. H. Scholz, and R. Bilham, On the mechanics of earthquake afterslip, *J. Geophys. Res.*, *96*, 8441–8452, 1991.
- Massonnet, D., W. Thatcher, and H. Vadon, Detection of postseismic fault-zone collapse following the Landers earthquake, *Nature*, *382*, 612–616, 1996.
- Miyazaki, S., P. Segall, J. Fukuda, and T. Kato, Space time distribution afterslip following the 2003 Tokachi-Oki earthquake: Implications for variations in fault zone frictional properties, *Geophys. Res. Lett.*, *31*, doi:10.1029/2003GL019410, 2004.
- Montési, L., Controls of shear zone rheology and tectonic loading on postseismic creep, *J. Geophys. Res.*, *109*, doi:10.1029/2003JB002925), 2004.

- Okada, Y., Internal deformation due to shear and tensile faults in a half-space, *Bull. Seismol. Soc. Am.*, *82*, 1018–1040, 1992.
- Peltzer, G., P. Rozen, F. Rogez, and K. Hudnut, Postseismic rebound in fault step-overs caused by pore fluid flow, *Science*, *272*, 1202–1204, 1996.
- Peltzer, G., P. Rozen, F. Rogez, and K. Hudnut, Poroelastic rebound along the Landers 1992 earthquake surface rupture, *J. Geophys. Res.*, *103*, 30,131–30,145, 1998.
- Perfettini, H., and J.-P. Avouac, Postseismic relaxation driven by brittle creep: A possible mechanism to reconcile geodetic measurements and the decay rate of aftershocks, application to the Chi-Chi earthquake, Taiwan, *J. Geophys. Res.*, *109*, doi:10.1029/2003JB002488, 2004.
- Perfettini, H., J. Schmittbuhl, and A. Cochard, Shear and normal load perturbations on a 2D continuous fault: 1. Static triggering, *J. Geophys. Res.*, *108*, doi:10.1029/2002JB001804, 2003.
- Perfettini, H., J.-P. Avouac, and J. Ruegg, Geodetic displacements and aftershocks following the 2001, $M_w = 8.4$ Peru earthquake: Implications for the mechanics of the earthquake cycle along subduction zones, *J. Geophys. Res.*, *109*, doi: 10.1029/2004JB003522, 2005.
- Pollitz, F., and I. Sacks, Stress triggering of the 1999 Hector Mine earthquake by transient deformation following the 1992 Landers earthquake, *Bull. Seismol. Soc. Am.*, *92*, 1487–1496, 2002.
- Pollitz, F., R. Burgmann, and P. Segall, Joint estimation of afterslip rate and postseismic relaxation following the 1989 Loma Prieta earthquake, *J. Geophys. Res.*, *103*, 26,975–26,992, 1998.

- Press, W. H., B. P. Flannery, S. A. Teukolsky, and W. T. Vetterling, Simulated Annealing Methods, in *Numerical Recipes in C, The Art of Scientific Computing, Second Edition*, pp. 451–455. Cambridge Univ. Press, Cambridge, England, 1992.
- Rice, J. R., Spatio-temporal complexity of slip on a fault, *J. Geophys. Res.*, *98*, 9885–9907, 1993.
- Rice, J. R., and J. Gu, Earthquake aftereffects and triggered seismic phenomena, *Pure Appl. Geophys.*, *121*, 187–219, 1983.
- Sauber, J., W. Tatcher, and S. Solomon, Geodetic measurement of deformation in central Mojave desert, California, *J. Geophys. Res.*, *91*, 12,683–12,693, 1986.
- Sauber, J., W. Tatcher, S. Solomon, and M. Lisowski, Geodetic slip rate for the eastern California shear zone and the recurrence time of Mojave desert earthquakes, *Nature*, *367*, 264–266, 1994.
- Savage, J., and J. Svarc, Postseismic deformation associated with the 1992 $M_w = 7.3$ Landers earthquake, southern California, *J. Geophys. Res.*, *102*, 7565–7577, 1997.
- Savage, J., M. Lisowski, and W. Prescott, An apparent shear zone trending north-northwest across the Mojave Desert into Owens Valley, eastern California, *Geophys. Res. Lett.*, *17*, 2113–2116, 1990.
- Savage, J., J. Svarc, and W. Prescott, Near-field postseismic deformation associated with the 1992 Landers and 1999 Hector Mine, California, earthquakes, *J. Geophys. Res.*, *108*, doi:10.1029/2002JB002330, 2003.
- Savage, J., J. Svarc, and S.-B. Yu, Postseismic relaxation and transient creep, *J. Geophys. Res.*, *110*, doi:10.1029/2005JB003687, 2005.

- Scholz, C. H., in *The Mechanics of Earthquakes and Faulting*. Cambridge Univ. Press, New York, 2002.
- Shen, Z.-K., D. Jackson, Y. Feng, M. Cline, M. Kim, P. Fang, and Y. Bock, Postseismic deformation following the Landers earthquake, California, 28 June 1992, *J. Geophys. Res.*, *84*, 780–791, 1994.
- Smith, S., and M. Wyss, Displacement on the San Andreas fault subsequent to the 1966 parkfield earthquake, *Bull. Seismol. Soc. Am.*, *58*, 1955–1973, 1968.
- Stein, R., The role of stress transfer in earthquake occurrence, *Nature*, *402*, 605–609, 1999.
- Wessel, P., and W. H. F. Smith, New, improved version of the Generic Mapping Tools released, *Eos Trans. AGU*, *79*, 579, 1998.
- Zweck, C., J. Freymueller, and S. Cohen, Three-dimensional elastic dislocation modeling of the postseismic response to the 1964 Alaska earthquake, *J. Geophys. Res.*, *107*, doi:10.1029/2001JB000409, 2002.

H. Perfettini, Institut de Recherche pour le Développement/Observatoire Midi-Pyrénées, 14 avenue Edouard Belin, 31400 Toulouse, France. (perfetti@lmtg.obs-mip.fr)

J.-P. Avouac, Tectonics Observatory, California Institute of Technology, Mail code 100-23, Pasadena CA 91125, USA. (avouac@gps.caltech.edu)

Received _____

to be submitted to *Journal of Geophysical Research*, 2006.

This manuscript was prepared with AGU's \LaTeX macros v5, with the extension package 'AGU++' by P. W. Daly, version 1.6a from 1999/05/21.

Figure Captions

Figure 1. Map of the Landers area showing the $M_w = 7.3$ Landers epicenter (blue star) and its aftershocks (blue dots: pre-Hector Mine seismicity; pink dots: post-Hector-Mine seismicity), the $M_w = 7.1$ Hector Mine epicenter (pink star), and the $M_w = 6.5$ Big Bear epicenter (red star). The white vectors show 6 years of postseismic surface displacements determined by USGS from GPS campaign measurements (white triangles) relative to GPS station Sanh [Savage and Svarc, 1997; Savage et al., 2003]. The red vectors show the corresponding displacements computed from our model. The box outlined with the dashed line is the zone used to represent the temporal evolution of seismicity in Figure 1b considering only the events with magnitude >2 , hence larger than the detection threshold [Hauksson et al., 2003]. The transparent lines show the simplified fault geometry of Fialko [2004b] used in this study.

Figure 2. Cumulated number of aftershocks in the near fault zone area outlined in the map and postseismic deformation as a function of time. Postseismic deformation is represented by the normalized function $f(t)$ characterizing the temporal evolution of surface displacements deduced from the principal component analysis of GPS times series [Savage and Svarc, 1997].

Figure 3. Coseismic slip (top) and modeled postseismic slip after 6 years of relaxation (bottom). The time evolution of afterslip is represented by isochrons. Each isochron encompasses the zone within which the cumulative slip exceeds 70 % of the peak slip at the considered time.

Figure 4. Influence of the parameter $a\sigma$ on the RMS in the vicinity of the best fit model.

Figure 5. Same as Figure 4 for the parameter V_0 .

Figure 6. Same as Figure 4 for the parameter V^- .

Figure 7. Same as Figure 4 for the parameter W_{bcfz} .

Figure 8. Measured and predicted horizontal displacements at site Sanh relative to stable North America. The contribution of the San Andreas fault system is taken into account [*Gordon et al.*, 1993].

Figure 9. Postseismic horizontal displacements from 1992 to 1999 relative to stable North America. Measurements are from USGS (blue symbols) [*Savage and Svarc*, 1997] were used in the inversion and the SCEC data (SOPAC:<http://sopac.ucsd.edu/dataArchive/>) (red symbols) were not. Black arrows show the velocities predicted by our model. Thick lines show the simplified fault geometry proposed by *Fialko* [2004b]. The green arrow has an amplitude of 15 cm.

Figure 10. Observed [*Savage and Svarc*, 1997] and modeled postseismic displacements relative to station Sanh. The east and north components of displacement are shown respectively by blue and black symbols. The continuous line represents the predictions of the best fitting model.

Figure 11. Coseismic Coulomb stress changes induced by the Landers mainshock computed at 10 km on right-lateral receiver faults striking N340°E.

Figure 12. Coulomb stress changes computed at the bottom of the seismogenic fault zone. The maps shows Coulomb stress changes on right-lateral faults striking N340°E computed at the top of the brittle creep fault zone, somewhat arbitrarily set to 15 km depth, induced by 0.06 yr (left) and 6 yr (right) of afterslip. Aftershocks with $M_L > 2$ over the same time period are also shown for comparison. See Figure 15 for cross-sections.

Figure 13. Map of Coulomb stress changes computed at depths of 5, 10 and 15 km on right-lateral receiver faults striking N340°E.

Figure 14. Locations of the lines AA', BB', CC' and DD' along which cross sections of Figure 15 are done. Also shown is the location of the boxes used to plot Figure 18.

Figure 15. Cross sections of Coulomb stress changes induced by afterslip along the profiles AA',BB',CC', and DD' of Figure S14. (Left panel): $6 \cdot 10^{-2}$ yr after the mainshock; (Right panel): 6 yr after the mainshock.

Figure 16. Agreement between the postseismic Coulomb stress change pattern of Figure 13 (center) and the distribution of aftershocks with $M_L > 2$ occurring within 6 years after the mainshock. See main text for details.

Figure 17. Same as Figure 16 for the coseismic Coulomb stress change pattern of Figure 11.

Figure 18. Normalized coulomb stress change computed at the center of the boxes of Figure S14 computed at the bottom of the SFZ together with the normalized cumulated number of aftershocks with $M_W > 2$ in the same boxes. The total number of aftershocks in each box during this 6 yr period is 3333 for box 1, 3412 for box 2, and 2219 for box 3.

Tables

Table 1. Correlation between the
Coulomb stress change pattern and the
location of aftershocks

Depth (km)	Coseismic	Postseismic
5	58.4 %	96.3 %
10	60.5 %	96.3 %
15	41.6 %	88.8 %

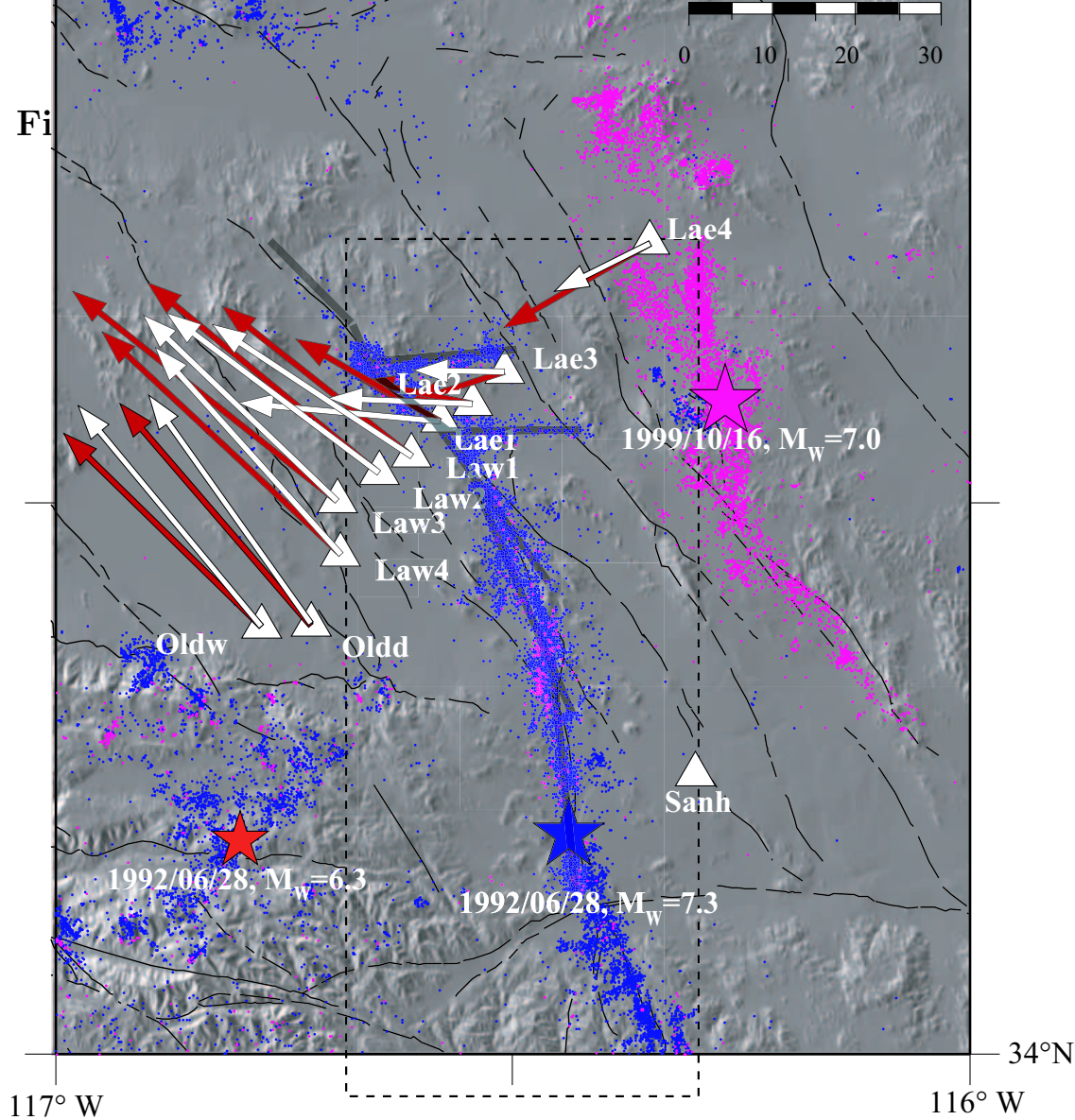


Figure 1. Map of the Landers area showing the $M_w = 7.3$ Landers epicenter (blue star) and its aftershocks (blue dots: pre-Hector Mine seismicity; pink dots: post-Hector-Mine seismicity), the $M_w = 7.1$ Hector Mine epicenter (pink star), and the $M_w = 6.5$ Big Bear epicenter (red star). The white vectors show 6 years of postseismic surface displacements determined by USGS from GPS campaign measurements (white triangles) relative to GPS station Sanh [Savage and Svare, 1997; Savage et al., 2003]. The red vectors show the corresponding displacements computed from our model. The box outlined with the dashed line is the zone used to represent the temporal evolution of seismicity in Figure 1b considering only the events with magnitude > 2 , hence larger than the detection threshold [Hauksson et al., 2003]. The transparent lines show the simplified fault geometry of Fialko [2004b] used in this study.

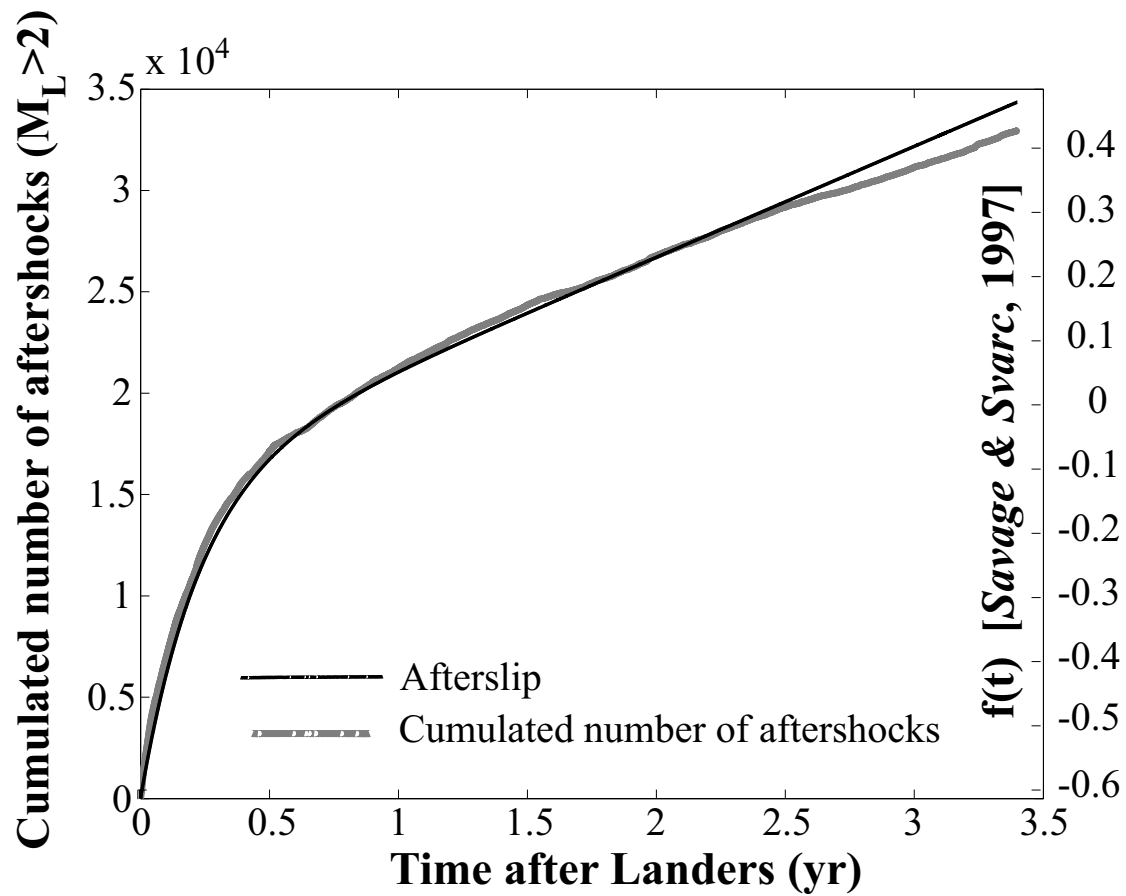


Figure 2. Cumulated number of aftershocks in the near fault zone area outlined in the map and postseismic deformation as a function of time. Postseismic deformation is represented by the normalized function $f(t)$ characterizing the temporal evolution of surface displacements deduced from the principal component analysis of GPS times series [Savage and Svarc, 1997].

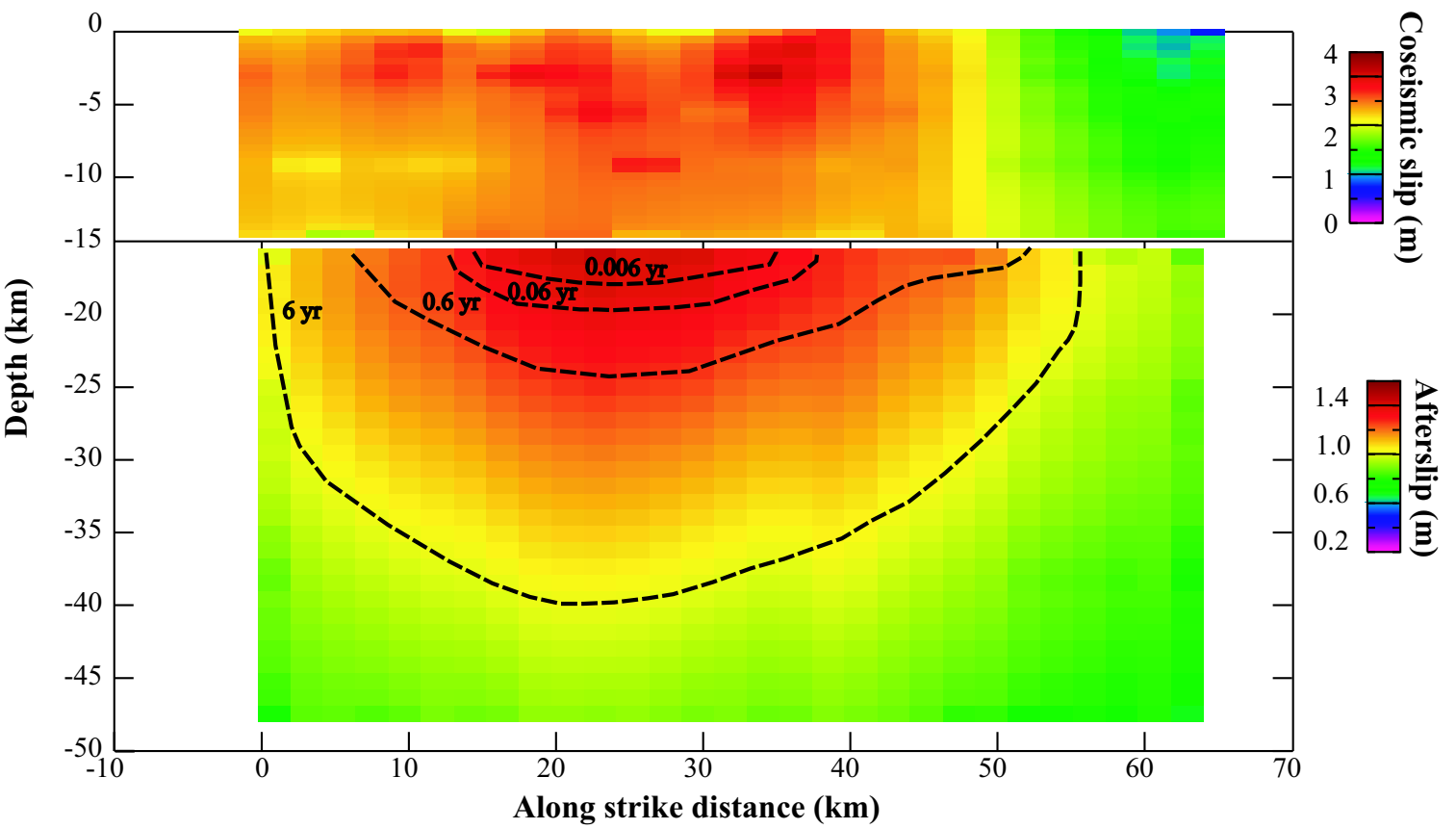


Figure 3. Coseismic slip (top) and modeled postseismic slip after 6 years of relaxation (bottom). The time evolution of afterslip is represented by isochrons. Each isochron encompasses the zone within which the cumulative slip exceeds 70 % of the peak slip at the considered time.

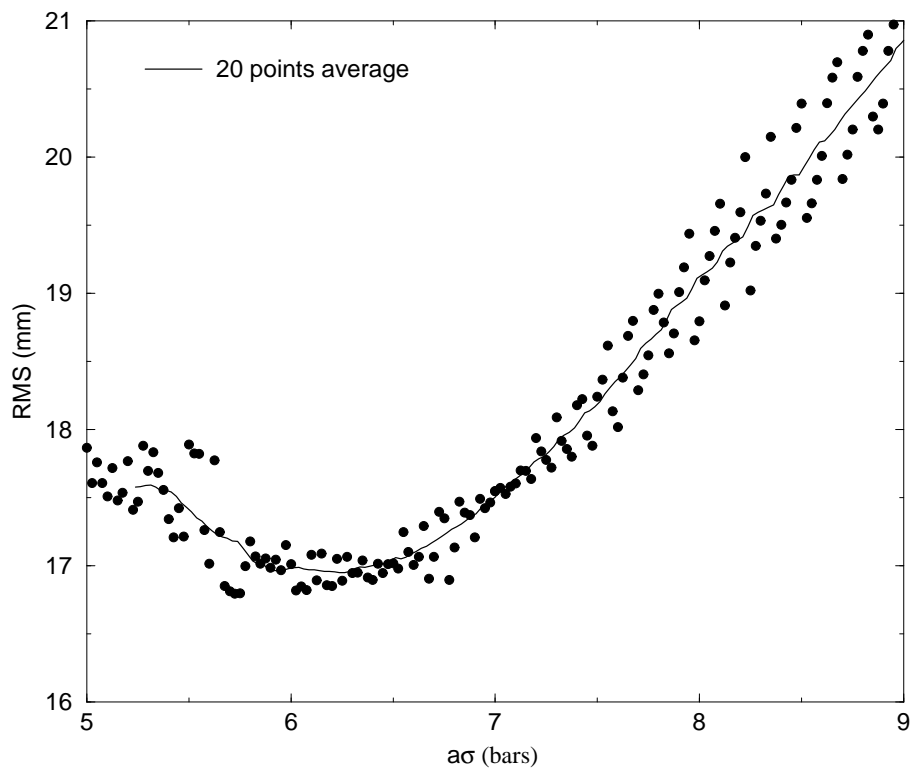


Figure 4. Influence of the parameter $a\sigma$ on the RMS in the vicinity of the best fit model.

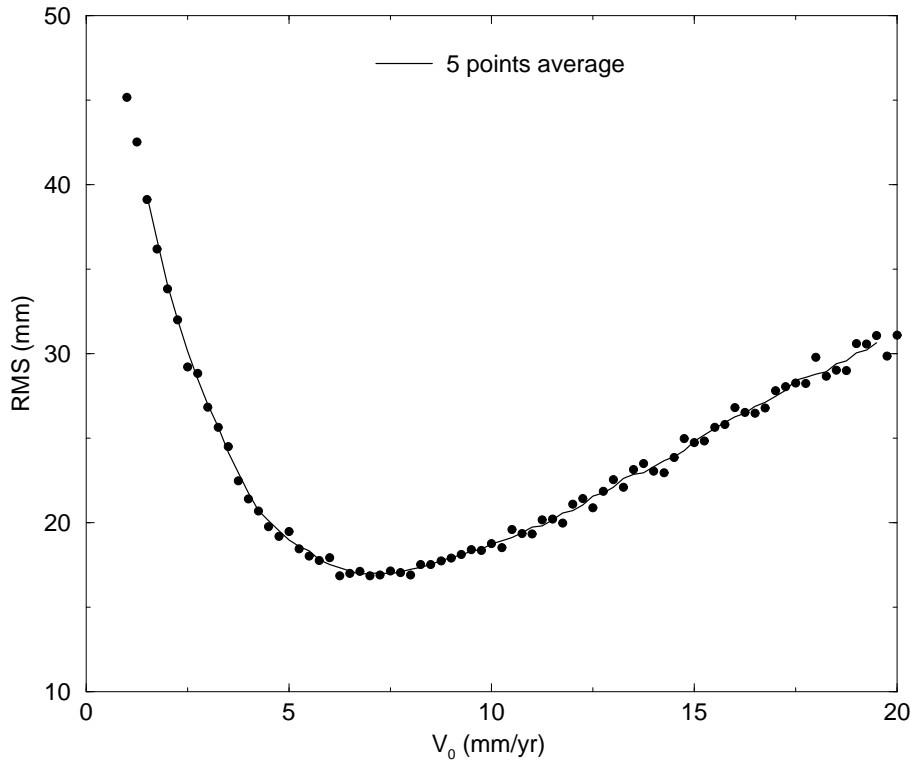


Figure 5. Same as Figure 4 for the parameter V_0 .

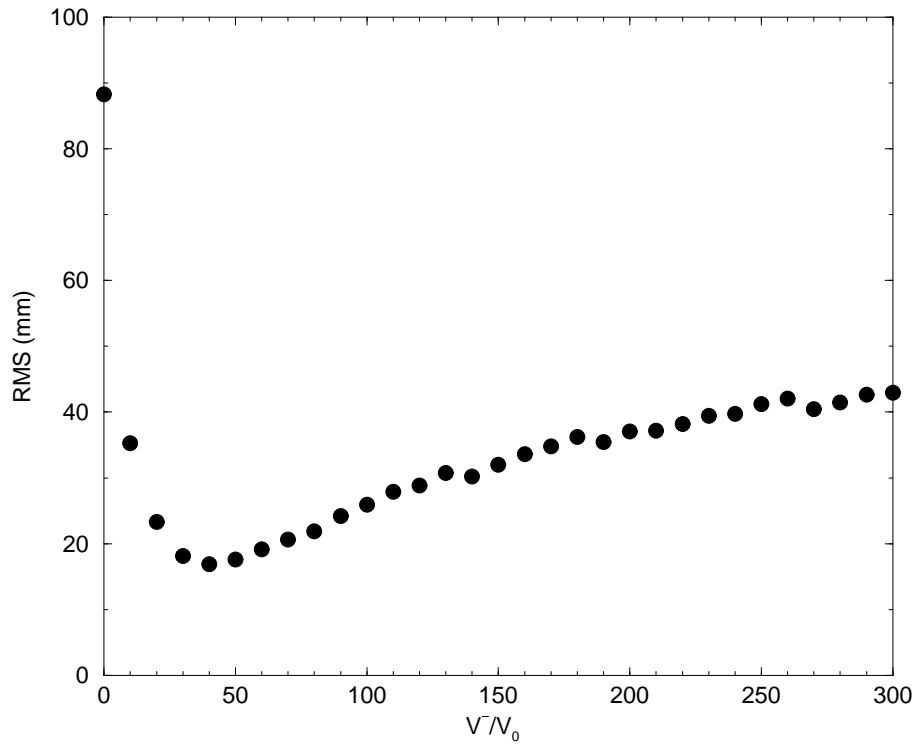


Figure 6. Same as Figure 4 for the parameter V^- .

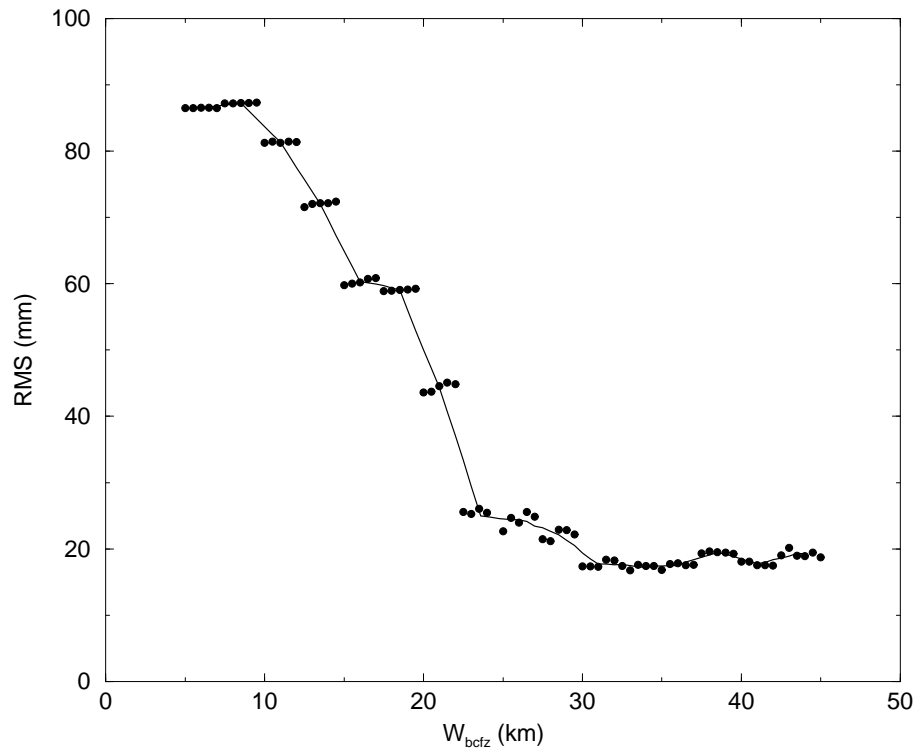


Figure 7. Same as Figure 4 for the parameter W_{bcfz} .

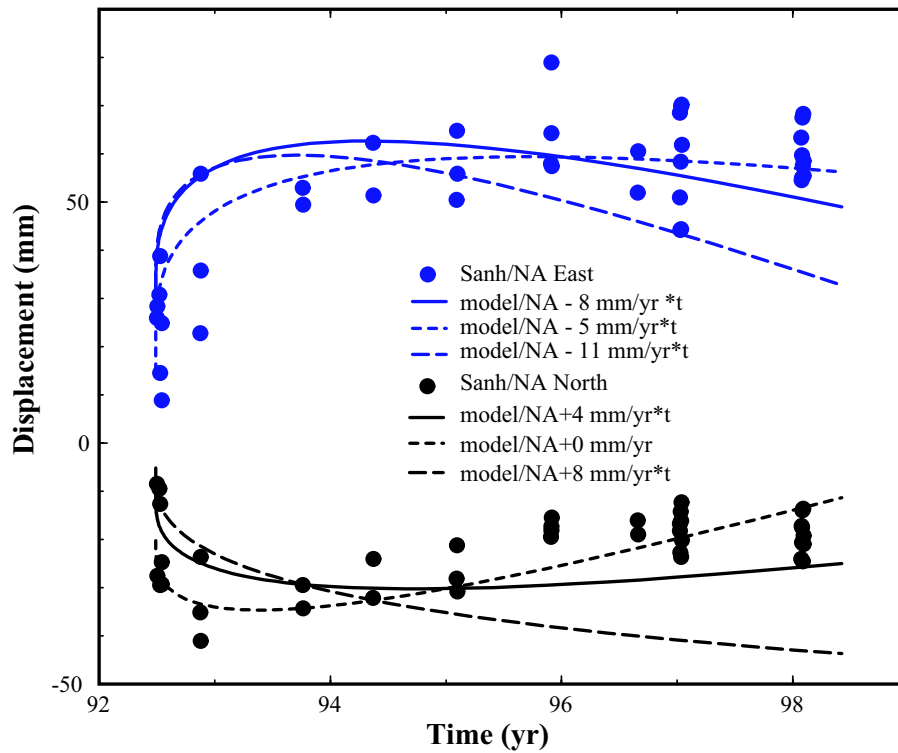


Figure 8. Measured and predicted horizontal displacements at site Sanh relative to stable North America. The contribution of the San Andreas fault system is taken into account [Gordon *et al.*, 1993].

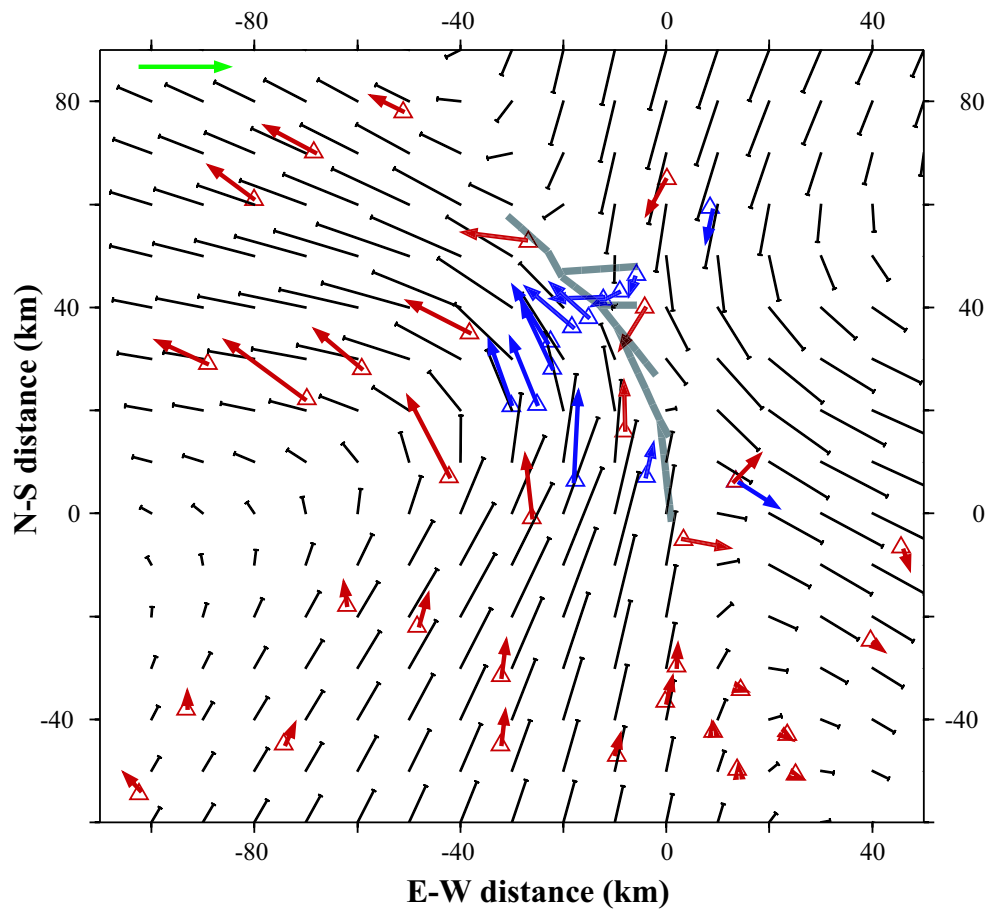


Figure 9. Postseismic horizontal displacements from 1992 to 1999 relative to stable North America. Measurements are from USGS (blue symbols) [Savage and Svarc, 1997] were used in the inversion and the SCEC data (SOPAC:<http://sopac.ucsd.edu/dataArchive/>) (red symbols) were not. Black arrows show the velocities predicted by our model. Thick lines show the simplified fault geometry proposed by Fialko [2004b]. The green arrow has an amplitude of 15 cm.

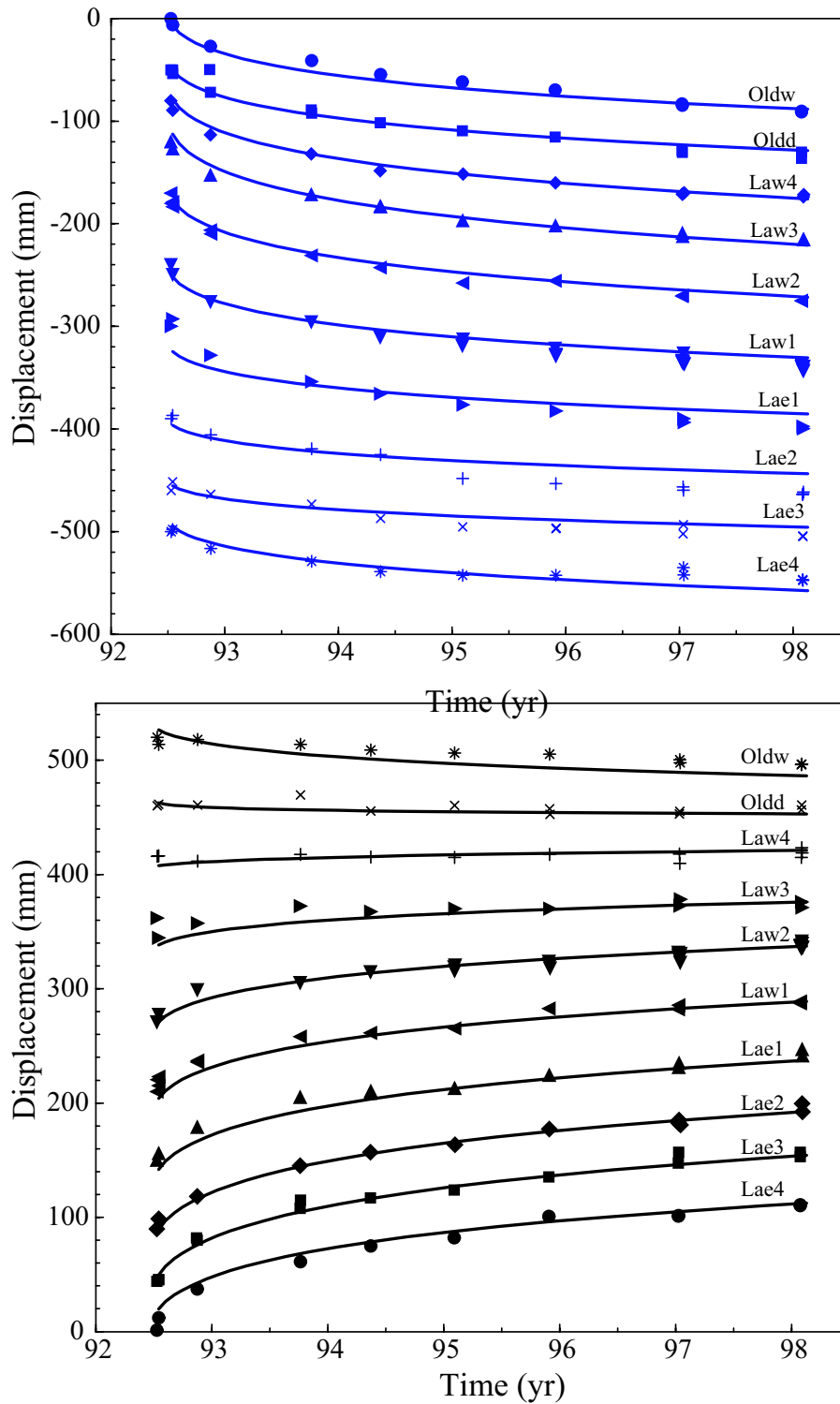


Figure 10. Observed [*Savage and Svarc, 1997*] and modeled postseismic displacements relative to station Sanh. The east and north components of displacement are shown respectively by blue and black symbols. The continuous line represents the predictions of the best fitting model.

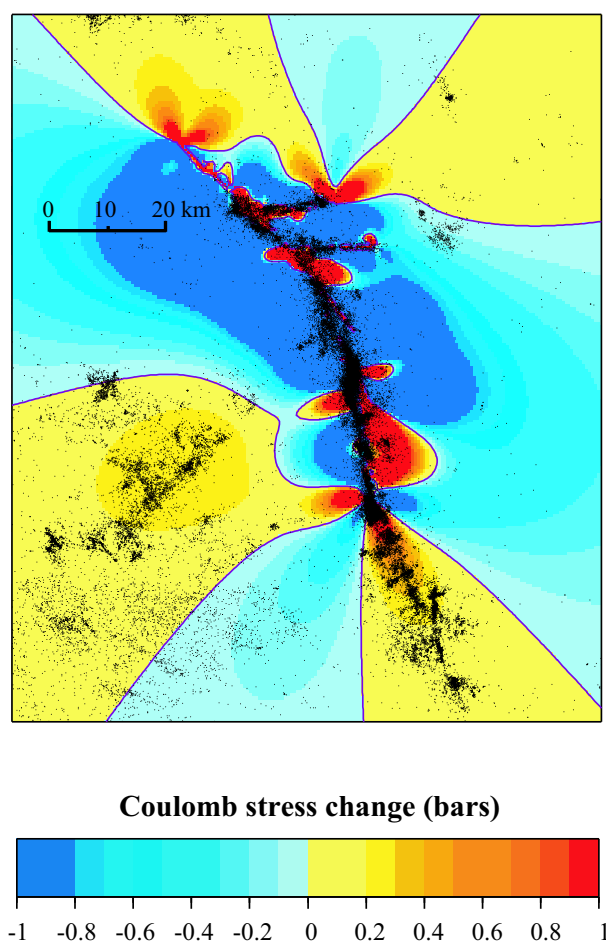


Figure 11. Coseismic Coulomb stress changes induced by the Landers mainshock computed at 10 km on right-lateral receiver faults striking $N340^{\circ}E$.

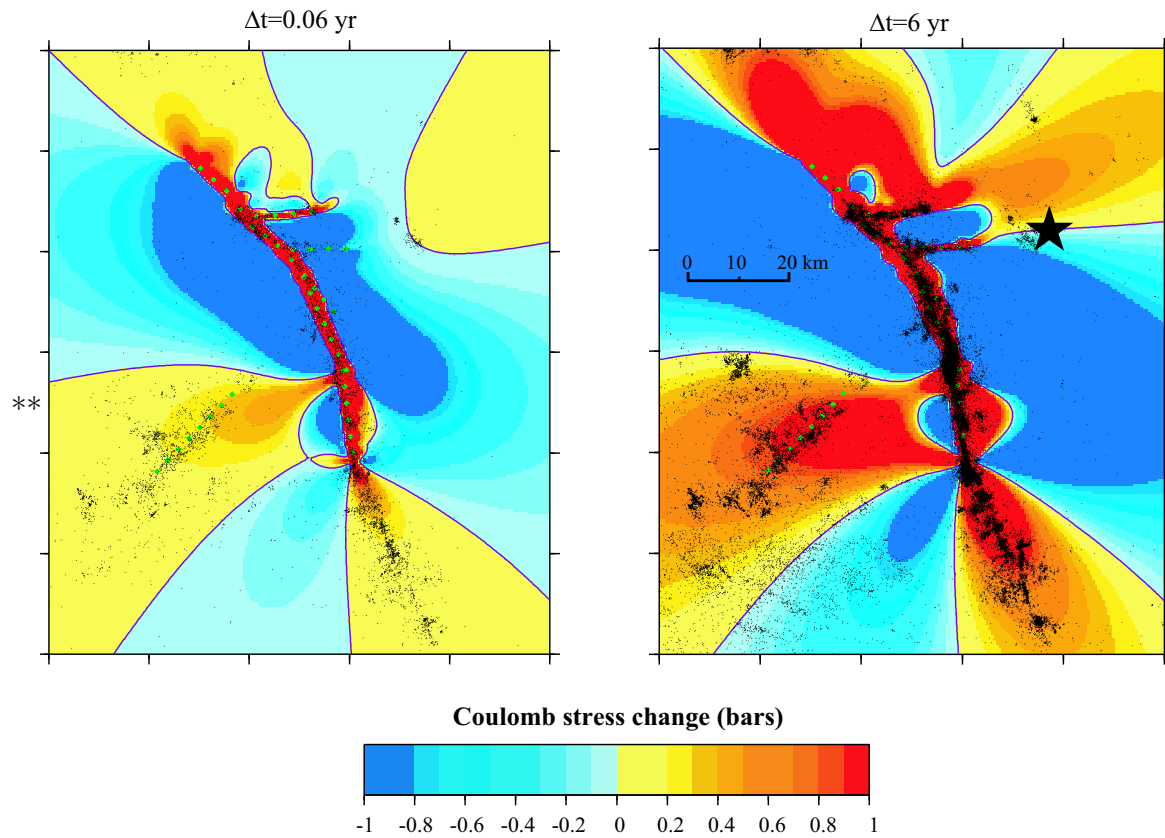


Figure 12. Coulomb stress changes computed at the bottom of the seismogenic fault zone. The maps show Coulomb stress changes on right-lateral faults striking N340°E computed at the top of the brittle creep fault zone, somewhat arbitrarily set to 15 km depth, induced by 0.06 yr (left) and 6 yr (right) of afterslip. Aftershocks with $M_L > 2$ over the same time period are also shown for comparison. See Figure 15 for cross-sections.

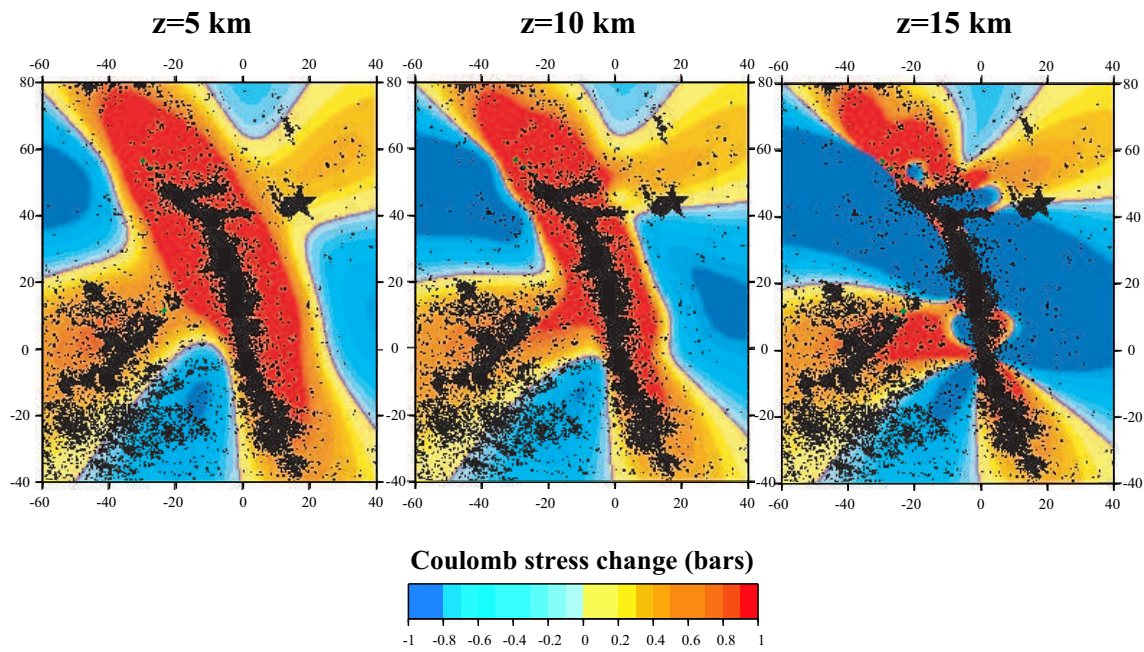


Figure 13. Map of Coulomb stress changes computed at depths of 5, 10 and 15 km on right-lateral receiver faults striking N340°E.

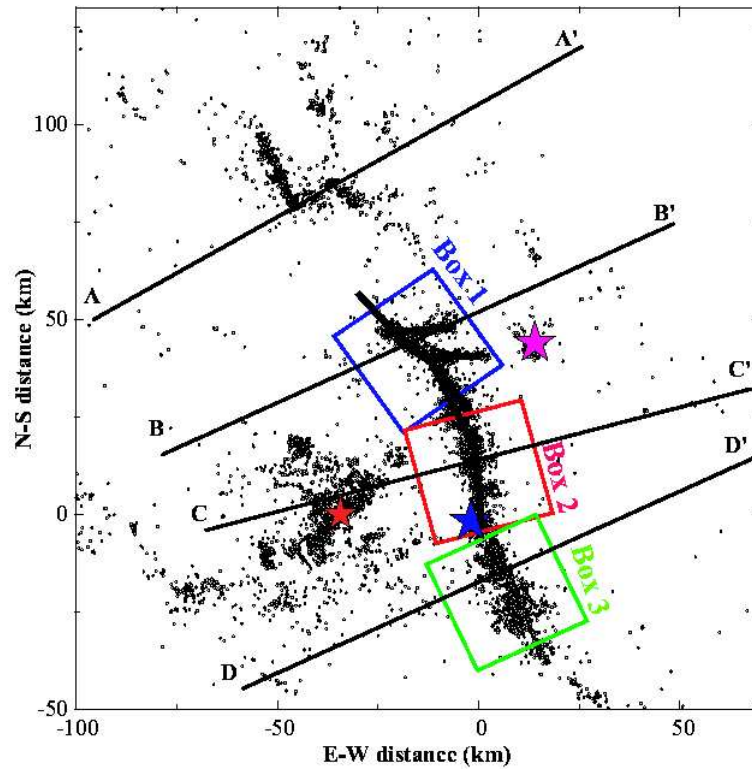


Figure 14. Locations of the lines AA', BB', CC' and DD' along which cross sections of Figure 15 are done. Also shown is the location of the boxes used to plot Figure 18.

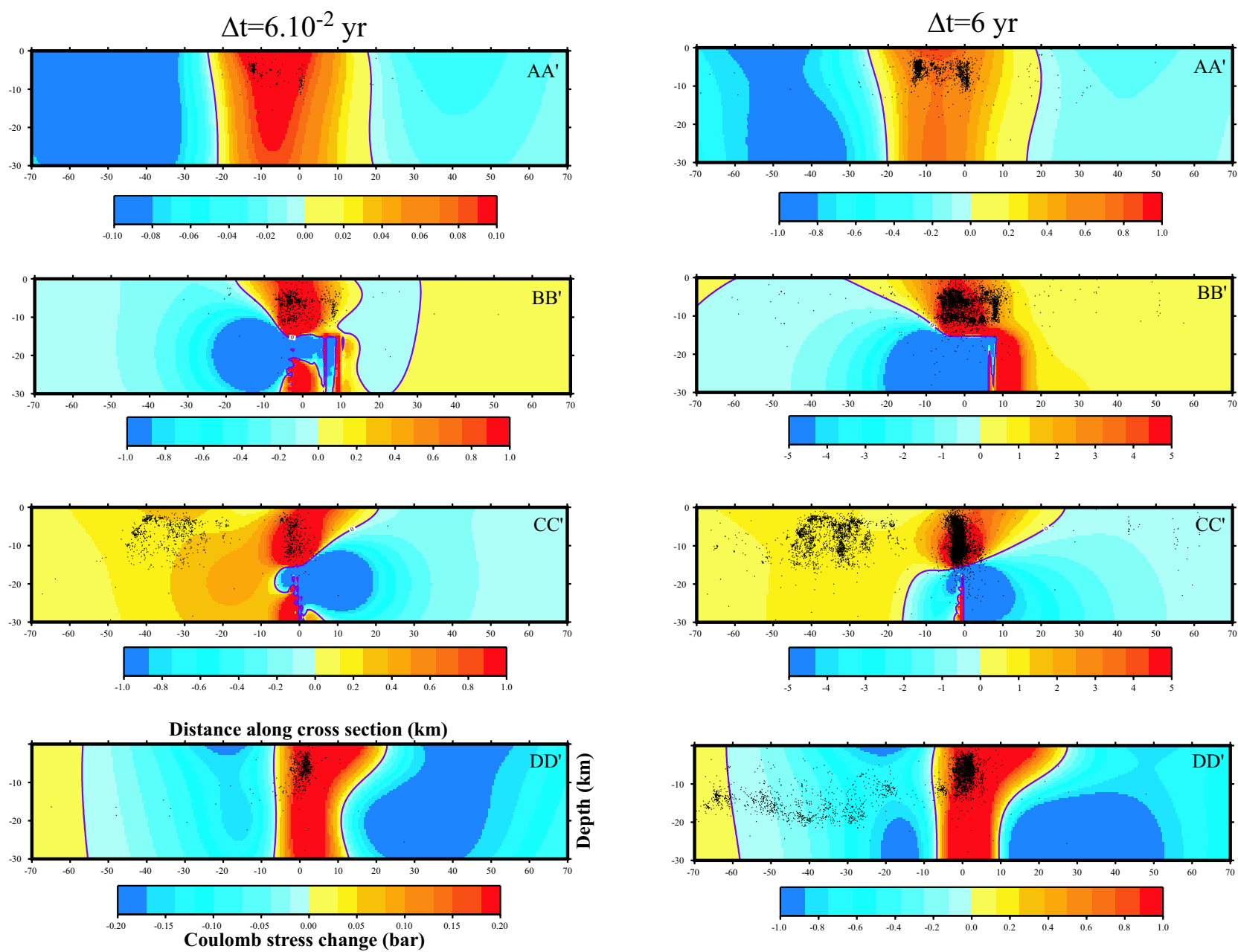


Figure 15. Cross sections of Coulomb stress changes induced by afterslip along the

profiles AA', BB', CC', and DD' of Figure S14. (Left panel): $6 \cdot 10^{-2}$ yr after the mainshock;

(Right panel): 6 yr after the mainshock.

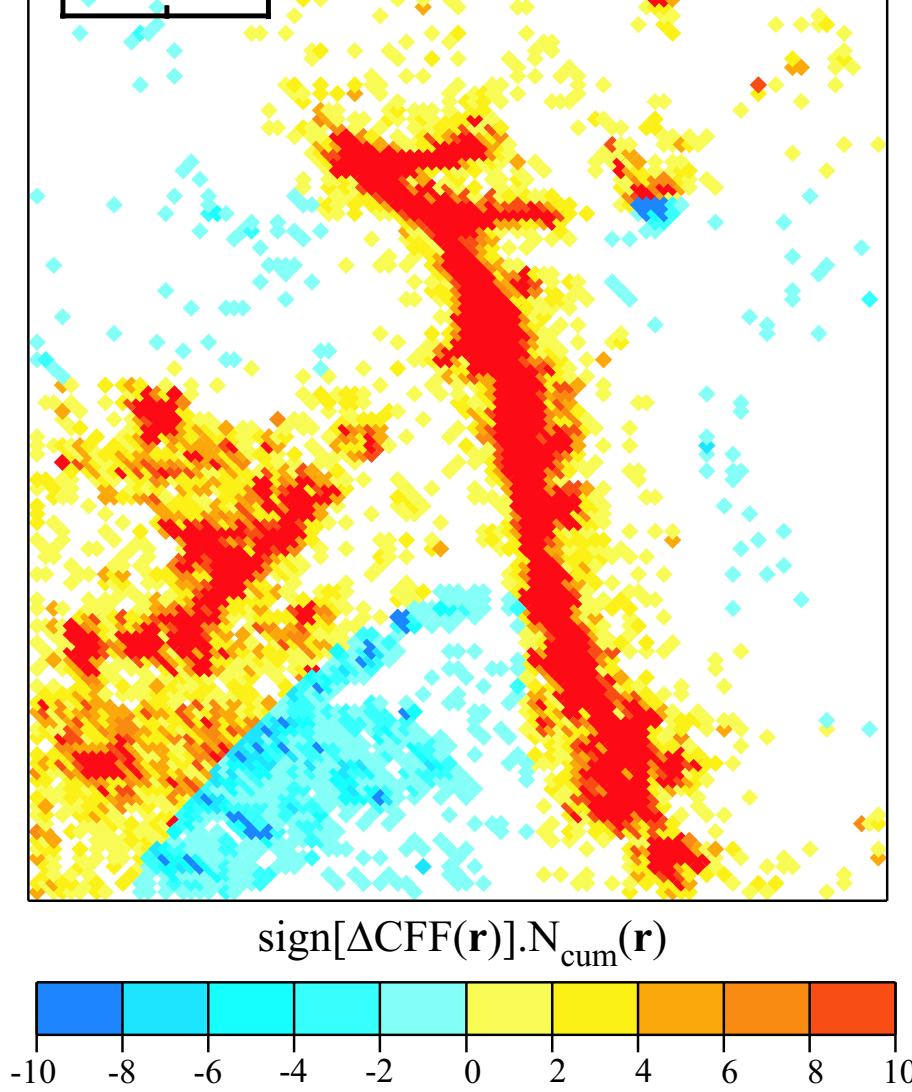


Figure 16. Agreement between the postseismic Coulomb stress change pattern of Figure 13 (center) and the distribution of aftershocks with $M_L > 2$ occurring within 6 years after the mainshock. See main text for details.

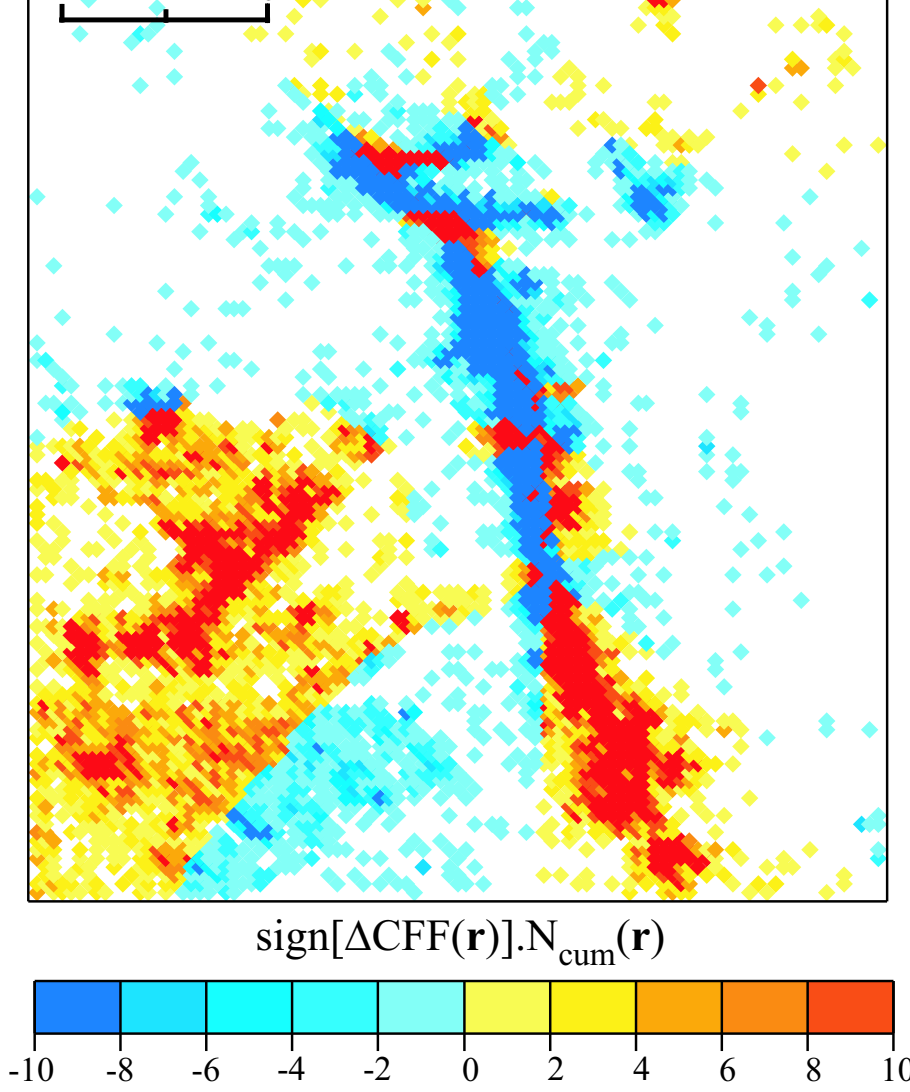


Figure 17. Same as Figure 16 for the coseismic Coulomb stress change pattern of Figure 11.

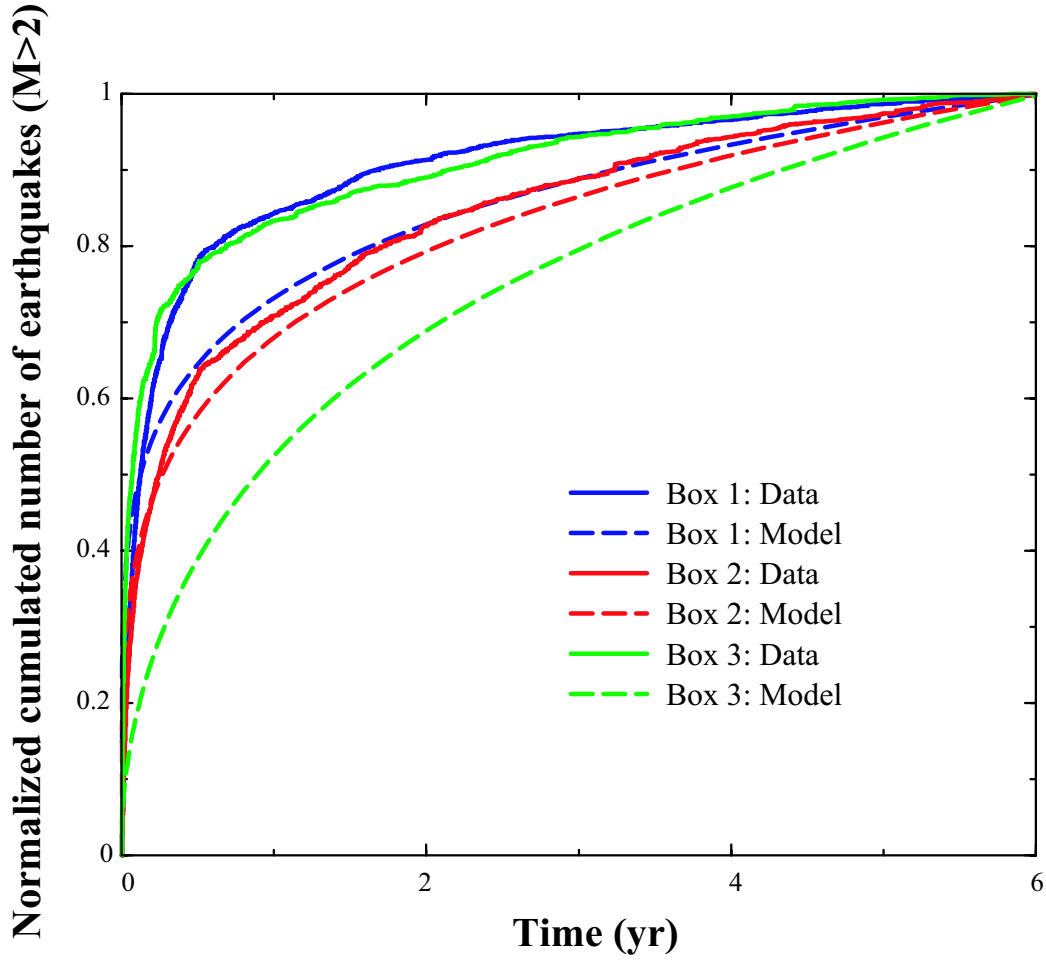


Figure 18. Normalized coulomb stress change computed at the center of the boxes of Figure S14 computed at the bottom of the SFZ together with the normalized cumulated number of aftershocks with $M_W > 2$ in the same boxes. The total number of aftershocks in each box during this 6 yr period is 3333 for box 1, 3412 for box 2, and 2219 for box 3.